On the Relationship Between Fault Permeability Increases, Induced Stress Perturbation, and the Growth of Aseismic Slip During Fluid Injection

Frédéric Cappa[1,2,3] iD, **Yves Guglielmi**[3] iD, **Christophe Nussbaum**[4], and **Jens Birkholzer**[3]

[1]Université Côte d'Azur, CNRS, Observatoire de la Côte d'Azur, IRD, Géoazur, Sophia Antipolis, France, [2]Institut Universitaire de France, Paris, France, [3]Energy Geoscience Division, Lawrence Berkeley National Laboratory, Berkeley, California, USA, [4]Federal Office of Topography, Swisstopo, St-Ursanne, Switzerland

Abstract Fluid injections into the deep subsurface can, at times, generate earthquakes, but often, they only produce aseismic deformations. Here we analyze the influence of fault hydromechanical properties on the growth of injection-induced aseismic slip. Using hydromechanical modeling, we show how permeability enhancement in addition to the background stress and frictional weakening has an important effect on the pressure diffusion and slip growth during injection. We find that the more pronounced the fault permeability enhancement, the stronger is the growth of the aseismic slip zone. The effect of enhanced permeability is more pronounced when the fault is initially close to failure. Our results show that aseismic slip grows beyond the pressurized zone when the fault permeability increases, while slip remains behind the pressurized zone when permeability does not vary from its initial preslip value. Thus, fault permeability increases should be considered as complementary mechanism to current models of fluid-induced aseismic slip.

Plain Language Summary Injection of fluid into the deep subsurface can, at times, generate measurable or even destructive earthquakes, but often, they only produce aseismic deformations along faults and fractures. The relationship between injected pressure and these aseismic deformations is a fundamental point in the estimation of how the crust responds to fluid injection and the associated induced seismic hazard. In this paper, we use data-driven hydromechanical modeling of fluid injection to show how the fault permeability enhancement in addition to the ambient stress and frictional weakening has an important effect on the fluid pressure diffusion, induced stress perturbation, and the growth of aseismic fault slip. Our results show that aseismic slip grows beyond the pressurized zone when the fault permeability increases, while slip remains behind the pressurized zone when permeability does not vary from its initial preslip value. Thus, fault permeability increases should be considered as complementary mechanism to current models of fluid-induced aseismic slip. These results help to further understand the complex behavior of fault slip caused by fluid injection in nature.

1. Introduction

During underground fluid injections, observations of measurable seismic events are generally explained by a direct response to the fluid pressure diffusion in a permeable fractured rock or a fault zone (Ellsworth, 2013; Keranen et al., 2014). Elevated fluid pressure can, indeed, lead to slip reactivation on preexisting fractures and faults when the Coulomb failure point is reached. Typically, the observed seismicity develops as a spatially expanding cloud around the injection zone. Sometimes, a quiet zone appears near the injection location once it has been subject to local reactivation, while the observed seismicity (and the injected fluids) continues to migrate away from the injection (Baisch et al., 2010). Interestingly, geothermal stimulations often show that the most energetic events occur during the phase of hydraulic unloading and at the spatial limit of the seismic cloud (Zang et al., 2014). During injection, earthquakes can also occur beyond the target reservoir both by poroelastic stressing (Goebel et al., 2016, 2017) and earthquake interactions (Catalli et al., 2016; Schoenball & Ellsworth, 2017).

However, fluid injections do not always generate earthquakes. Quite frequently, fluid injections result in aseismic slip, propagating slowly without any measurable seismic activity (Cornet, 2016; Duboeuf et al., 2017; Guglielmi, Cappa, et al., 2015; Lengliné et al., 2017; Wei et al., 2015). Such aseismic slip can weaken

the fault, which, in turn, may fail later in a larger earthquake. This process therefore provides an alternative mechanism for triggering and driving injection-induced seismicity (Guglielmi, Cappa, et al., 2015; Wei et al., 2015). Understanding the growth of such aseismic slip is thus crucial to better assess the induced seismicity hazard.

Furthermore, experimental studies indicate that the simultaneous changes in hydraulic diffusivity and friction during fluid injection influence the fault slip modes, aseismic or seismic, upon fault reactivation (Guglielmi, Elsworth, et al., 2015; Scuderi et al., 2017; Scuderi & Collettini, 2016). Therefore, understanding how the hydraulic and frictional properties of a fault evolve during fluid injection is crucial in predicting its slip behavior and the spatial extent of slip relative to the pressurized zone.

In this study, we focus on injection-induced "aseismic" slip and, in particular, how the enhancement of fault permeability influences the growth of slip. To unravel potential controls on aseismic slip, we first revisit the evolution of fault permeability associated with aseismic deformations observed during an in situ experiment of fluid injection into a densely instrumented fault in a carbonate formation (Guglielmi, Cappa, et al., 2015). Second, we conduct coupled hydromechanical simulations of fluid injection in a single planar fault under stress and fluid pressure conditions similar to those found in the in situ experiment. We focus on the effect of the change in fault permeability for different initial stress conditions and friction laws to elucidate how this may affect the growth of aseismic slip.

2. Observation of Fault Permeability Enhancement During Fluid Injection Experiments

Guglielmi, Cappa, et al. (2015) have previously shown that the observation of fault displacements during fluid injection implies that permeability varies in close relation to the evolution of fluid pressure. Their paper describes a controlled injection experiment conducted at 282-m depth into a natural fault (slip offset of a few meters) in a carbonate formation, with a simultaneous monitoring of fluid pressure, flow rate, and fault deformation at the injection location, as well as seismicity monitored nearby (Figure 1). Based on this data set, Guglielmi, Cappa, et al. (2015) and Guglielmi, Elsworth, et al. (2015) determined the evolution of fault permeability using a hydromechanical model calibrated to both the fluid pressure and flow rate measured at the injection location. The model assumes that the perturbations in fluid pressure result in lateral diffusion along the fault from the injection. Thus, the model represents pressure and permeability gradients that decrease at larger distances from the injection. In the model, the calculated permeability k (m^2) is expressed in terms of hydraulic aperture b_h (m) based on the cubic law (Witherspoon et al., 1980), which links the change in fluid pressure ΔP (Pa) and flow rate ΔQ (m^3/s):

$$b_h = -\left(\frac{12\mu_f \cdot \Delta Q}{w \cdot \Delta P}\right)^{\frac{1}{3}} \text{ and } k = \frac{b_h^2}{12} \tag{1}$$

where μ_f is the viscosity of fluid (Pa.s) and w is the fault width (m). In a parametric analysis, we find values of hydraulic aperture that minimize the misfit between model predictions and observed pressure and flow rate histories at the injection point. The permeability is then defined from the best fit value of hydraulic aperture. Thus, this experiment offers ideal conditions to evaluate how fault permeability evolves with accumulated displacements, both during aseismic deformation and seismic activity, and to constrain further hydromechanical modeling analyses of fault slip (see section 4).

Observations showed a complex interplay between fluid pressure, fault deformation, and fault permeability change. Guglielmi, Cappa, et al. (2015) showed that the increase in fluid pressure induces fault opening and aseismic slip at the injection. The seismicity is then triggered indirectly at a distance from injection by stress transfer associated with propagating aseismic slip. Duboeuf et al. (2017) confirmed this mechanism in a series of 11 injection experiments at the same site. In these experiments, seismic events were located between 1 and 12 m from the injection points where the measured fault slip is aseismic. Then, Guglielmi, Cappa, et al. (2015) found a 14-fold increase of the fault permeability from 0.07 to 1.0×10^{-10} m^2 during the period of aseismic slip, representing about 70% of the total cumulative permeability increase (20-fold) during the injection period (Figure 1). In contrast, during a subsequent period of seismic activity at a distance from injection, the fault permeability only increases from 1.0×10^{-10} to 1.35×10^{-10} m^2. Hence, these detailed observations
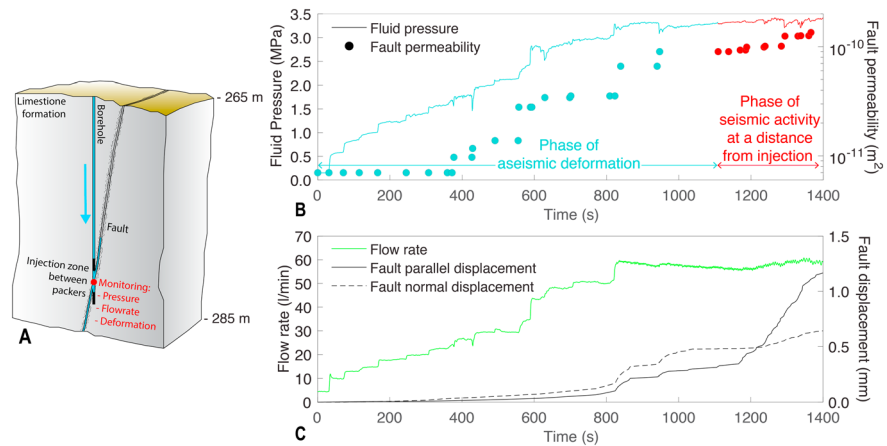
Figure 1. (a) Diagram of the experiment. Water is injected between packers in the fault with simultaneous monitoring of fluid pressure, flow rate, and fault displacement (Guglielmi, Cappa, et al., 2015). (b) Evolution of fluid pressure and fault permeability during a fluid injection into the fault. The light blue color corresponds to the period of aseismic deformation (0 to 1,100 s), while the red color is indicative of the period of seismic activity (1,100 to 1,400 s). In this experiment, fault slip is aseismic at injection, while seismic events are triggered at a distance from injection, in the fractured volume that surrounds the fluid-pressurized fault (Duboeuf et al., 2017; Guglielmi, Cappa, et al., 2015). (c) Evolution of flow rate, fault normal (i.e., "opening"), and fault parallel (i.e., "slip") displacements during the injection.

of fault permeability enhancement during fault activation highlight that the evolution of fault hydraulic parameters is essential to understand the growth of slip during fluid injection. Clearly, the increase in fluid pressure induces fault opening and slip that cause permeability changes. Then, the different modes of fault permeability changes seem to influence the slip behavior.

3. Hydromechanical Modeling of Fault Slip by Fluid Injection

3.1. Model Setup

To investigate the effect of fault permeability enhancement on the growth of aseismic slip during fluid injection, we use the 3DEC code (Itasca Consulting Group, 2016), a distinct element method (Cundall, 1988), to simulate the interaction between fluid flow and fault slip evolution, including hydromechanical coupling, effective stress, and friction laws (Text S1 in the supporting information). The model uses the cubic law (1) to describe the coupling between the fluid pressure diffusion and the permeability change caused by the normal displacement of the fault (Witherspoon et al., 1980). The hydraulic aperture (b_h) can vary (1) as a function of the change in effective normal stress ($\Delta\sigma_n' = \Delta\sigma_n + \Delta P$, with σ_n is the total normal stress) and (2) as a function of dilation caused by shear slip ($b_{hs} = \Delta u_s \cdot \tan\psi$) along a planar fault (i.e., no roughness):

$$b_h = b_{ho} + \frac{\Delta\sigma_n'}{k_n} + \Delta u_s \cdot \tan\psi \tag{2}$$

where b_{ho} (m) is the initial aperture at zero normal stress, k_n is the fault normal stiffness (Pa/m), u_s (m) is the shear slip, and ψ is the dilation angle (°).

The method has been previously used to evaluate the hydromechanical behavior of fractured rocks and fault zones during fluid pressurization (Cappa et al., 2006; Guglielmi et al., 2008), showing that the evolution of fault hydraulic diffusivity is a fully coupled problem depending on stress and fluid pressure (Guglielmi, Elsworth, et al., 2015).

We select a simplified yet representative 2-D model (200 m × 50 m) that considers fluid injection into a horizontal flat fault in a homogeneous elastic and impervious medium (Figure 2a). The remote normal (σ_n) and shear stress (τ) resolved on the fault plane are constant. During injection, the fluid pressure in the fault is increased step by step in 0.5-MPa increments every 150 s. Injection occurs in a point source (Figure 2a) in order to reproduce a loading path consistent with the in situ data presented in Figure 1. The total time of
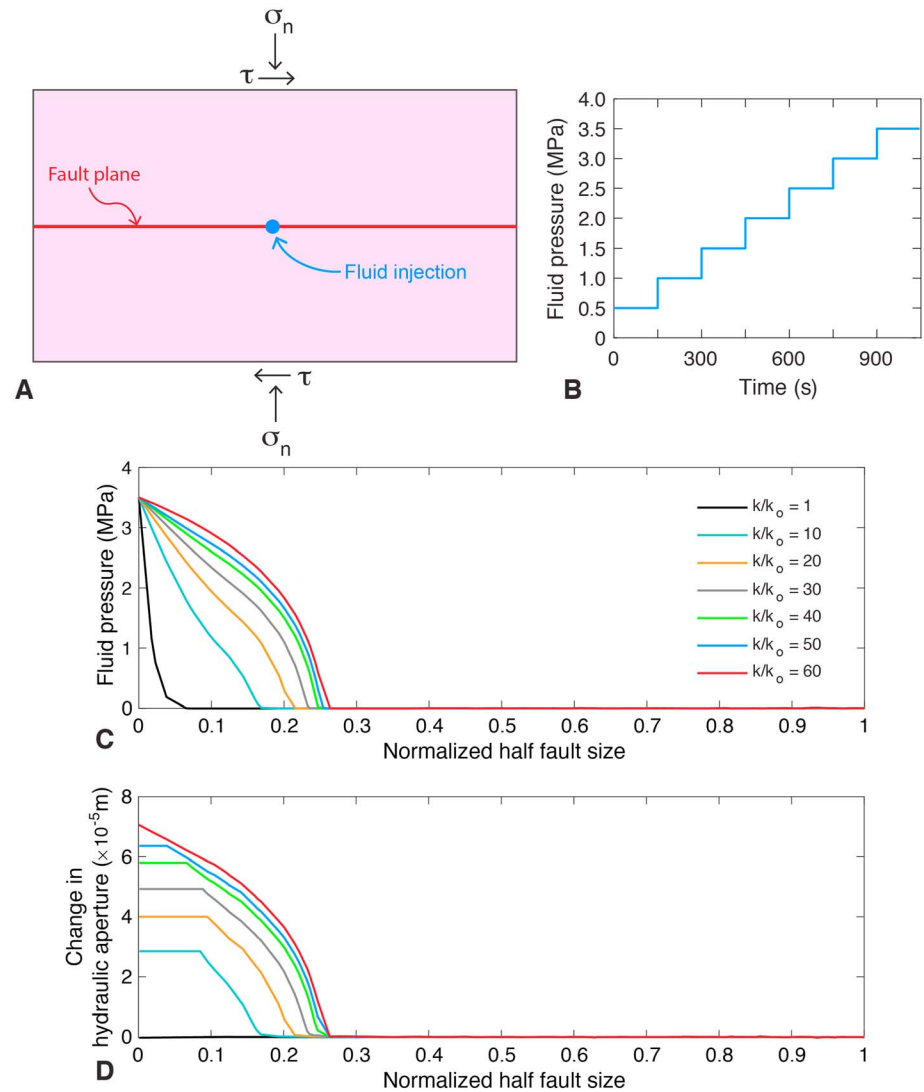
Figure 2. (a) Model geometry and (b) injection scenario into the fault. The remote normal (σ_n) and shear stress (τ) resolved on the fault plane are constant. Half-profiles of (c) fluid pressure and (d) hydraulic aperture calculated along the fault assuming different permeability changes. The injection point is located at $x = 0$ along the horizontal axis. Half-profiles are plotted at the end of injection.

injection is 1,050 s. We focus on the period of largest increase of fault permeability observed in the in situ experiment (Figure 1b). For numerical accuracy, the mesh size is refined along the fault (0.15 m) and gradually increases to 0.5 m in the direction normal to the fault toward model boundaries.

The initial values of normal stress ($\sigma_{no} = 4.25$ MPa) and fluid pressure ($p_o = 0$ MPa) in the fault represent the conditions of the in situ experiment (Duboeuf et al., 2017; Guglielmi, Cappa, et al., 2015). We used two different values of shear stress ($\tau_o = 1.65$ and 2 MPa) to have different levels of fault criticality to failure, $\tau_o/\sigma_{no} = 0.388$ and 0.47, respectively. We also tested different factors of permeability changes with fault displacements ($k/k_o = 1, 10, 20, 30, 40, 50,$ and 60). Thus, the permeability can vary between a prescribed initial value (k_o) and a capped maximum value (k). The effect of shear-induced dilation (b_{hs}) was investigated for different values of dilation angle ($\psi = 0$ to 2.5°). The fault hydraulic properties and the rock elastic properties were taken from previous studies on the same fault zone (Derode et al., 2015; Guglielmi, Cappa, et al., 2015). The initial hydraulic aperture is assumed to be 9.15 μm (i.e., $k_o = 7 \times 10^{-12}$ m²). Rock elastic properties are $K = 20$ GPa for the bulk modulus and $G = 9$ GPa for the shear modulus (Jeanne et al., 2012).

Here we model a slow aseismic slip either with constant friction or rate-and-state friction (Marone, 1998). In our simulations, the slip is aseismic because the maximum slip velocity along the fault (~0.45 mm/s) is below a typical threshold of dynamic (i.e., seismic) slip velocity (5 mm/s to 0.1 m/s; Gischig, 2015; McClure & Horne, 2011) defined by the rock elastic properties and the fault frictional properties (Rubin & Ampuero, 2005). Slip initiates based on the Mohr-Coulomb failure criterion ($\tau = \mu \cdot \sigma_n'$, where τ is the shear stress at which slip initiates and μ is the friction coefficient; Jaeger & Cook, 1979). When fault slips, the slip velocity (v) dependence of friction is defined using the Dieterich type evolution equation (Dieterich, 1979; Marone, 1998):

$$\mu(v, \theta) = \mu_0 + a \, \ln\left(\frac{v}{v_0}\right) + b \, \ln\left(\frac{v_0 \theta}{D_c}\right), \text{with} \quad \frac{d\theta}{dt} = 1 - \frac{v\theta}{d_c} \tag{3}$$

We use the following frictional parameters, $\mu_o = 0.6$, $(a\text{-}b) = -0.002$, and $d_c = 10\ \mu\text{m}$. These values fall within the range of frictional parameters measured in laboratory tests on fault samples collected in carbonate rocks (Carpenter et al., 2014, 2016). μ_o is the friction coefficient at a reference slip velocity (v_o). The parameter a quantifies the direct effect of a change in slip velocity. The parameter b describes the effect of the state variable (here we use the "aging law"; Dieterich, 1979). The characteristic slip distance, d_c, governs the evolution of the state variable (θ). For fault models with constant friction, we assume a static value (μ_s) of 0.6.

3.2. Modeling Results

Figures 2c and 2d show how the development of the fluid pressure along the fault varies as a function of the permeability enhancement factor and the associated hydraulic aperture. Models indicate that the magnitude and distribution of the steady state overpressure as well as the size of the pressurized area depend strongly on the permeability change. For a constant permeability model (case $k/k_o = 1$), the pressure perturbation is poorly pronounced. The highest pressure and sharpest pressure gradients are located close to the injection. For models with changing permeability during slip, the size of the pressurized zone grows significantly with the fault permeability enhancement. Models show that the higher the permeability increase, the greater is the pressurized area (Figure 2c). The permeability increase is higher near the injection and decreases at larger distances (Figure 2d). We define the pressurized length of the fault as the distance from the injection to the limit of the pressurized zone where the fluid pressure is zero (this distance is then normalized by the fault length). Given the applied injection pressure and the resulting calculated fault deformation, the pressurized length reaches a maximum normalized value of 0.2635.

Our model results also indicate that the permeability evolution affects both the maximum diffusion length and the size of the slip zone (Figures 3a and 3b). The extent of the slip zone is defined as the distance between the injection and the limit of the slipping patch where the slip is zero. Figures 3a and 3b suggest that the larger the increase in fault permeability, the larger is the extent of the slip zone. When a sufficient portion of the fault is pressurized and weakened, fault slip accelerates (i.e., slow stick-slip, Figure S1 in the supporting information), and a step-like increase in the length of the slip zone occurs. The most pronounced difference between the slip and pressure fronts occurs for the higher, more critical, initial stress ratio ($\tau_o/\sigma_{no} = 0.47$). For this case, results highlight that all simulations including permeability changes ($k/k_o > 1$) show that the growth of fault slip outpaces the growing fluid pressure front. For a less critical initial stress ratio ($\tau_o/\sigma_{no} = 0.388$), results show that the growth of fault slip outpaces the growing fluid pressure front for permeability changes (k/k_o) greater than 10. For the highest permeability enhancement ($k/k_o = 60$), the size of the slip zone is about 1.74 and 3.23 greater than the size of the pressurized zone, respectively, for initial stress ratios of 0.388 and 0.47 (Figure 4).

In Figures 3c and 3d, we compare the slip length as a function of the length of the pressurized zone for different stress ratio (τ_o/σ_{no}) and different friction laws for the case with the highest permeability increase ($k/k_o = 60$). We find that the growth of slip is affected both by the background stress and frictional weakening. For example, a fault with higher background stress ($\tau_o/\sigma_{no} = 0.47$) can produce larger slip growth (Figure 3c). The background stress affects both the timing of the slip front outpacing the fluid diffusion front and the subsequent size evolution of slip area (Figure 3d). Reducing the shear stress delays the timing of the slip front outpacing the fluid diffusion front (734 s in Figure 3d) and decreases the maximal size of slip area, whereas increased shear stress leads to earlier onset (471 s in Figure 3d) and a larger slip zone. The effect of fault friction is also illustrated in Figures 3c and 3d. Fault frictional weakening using the rate-and-state friction law
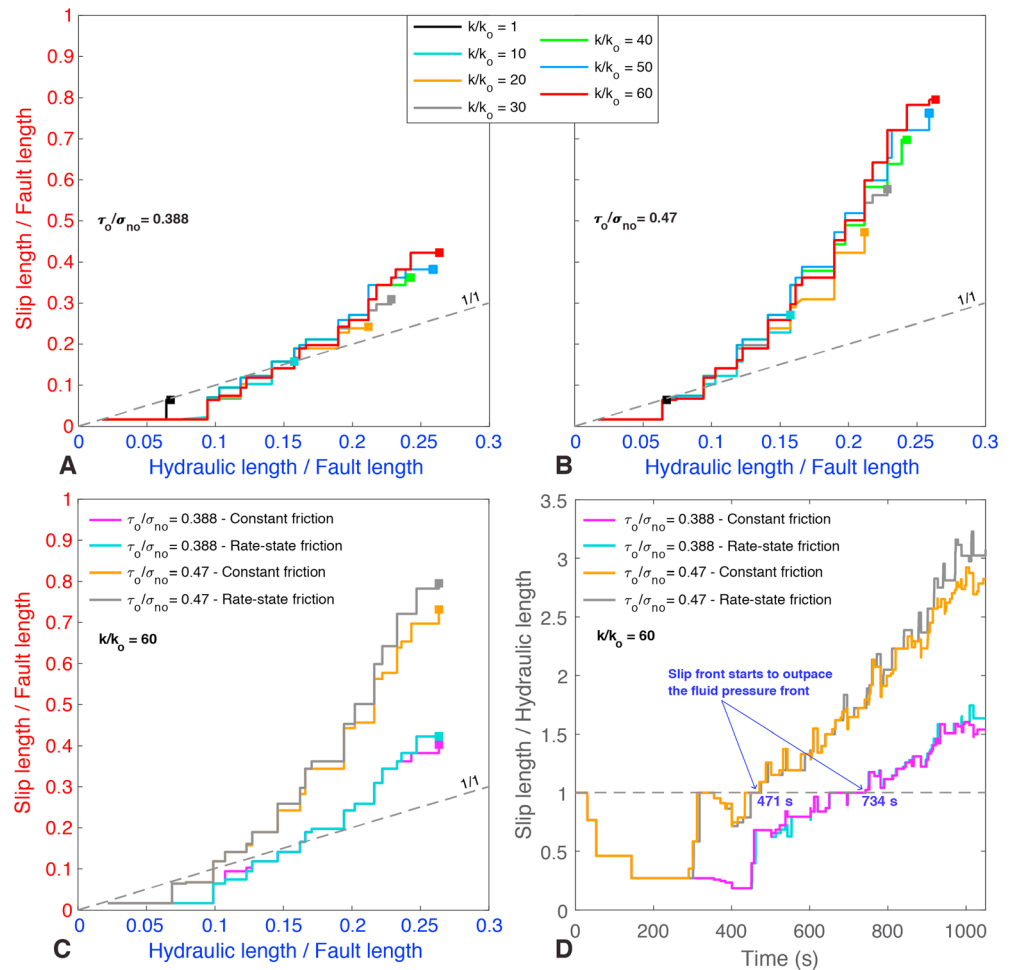
Figure 3. Influence of stress conditions and fault-related frictional and hydraulic parameters on the evolution of fault slip. Slip length as function of the hydraulic length (i.e., distance relative to the injection normalized by the half-length of the fault) for different changes in fault permeability and for two stress regimes, (a) $\tau_o/\sigma_{no} = 0.388$ and (b) $\tau_o/\sigma_{no} = 0.47$, respectively. (c) Slip length as function of the hydraulic length and (d) ratio of the slip length to hydraulic length with time, for different initial stress ratios and friction laws (i.e., constant friction and rate-and-state friction).

influences the temporal evolution of the slipping area and may produce larger ruptures. This is expected because friction weakening leads to reduced fault strength with sequences of accelerated and increased slip, while constant friction tends to stabilize fault strength resulting in less pronounced slip (Figure S1).

The possible role that the fault dilatancy may play is investigated by testing different values of dilation angle ($\psi = 0$ or 2.5°). By comparison with the simulations neglecting the effect of shear-induced dilation ($\psi = 0$), results indicate that even a large dilation angle ($\psi = 2.5°$), which ensures strong coupling between fault slip and hydraulic aperture (Gischig, 2015), has only a minor effect on the size of the pressurized and slip zones (Figure S3). The results show that a large shear-induced dilation increases the hydraulic length only by 3% (case with $\tau_o/\sigma_{no} = 0.47$) and the slip length by 1% compared to a case without shear-induced dilation. These results also show that the simulation outcomes are not very sensitive to the permeability dependence on shear slip, likely due to the high initial permeability, and that the permeability change is mainly controlled by the evolution of the effective normal stress.

In summary, the change in fault permeability and the initial stress state on the fault have an important impact on fault slip that can occur over a zone greater than the fluid-pressurized zone. In addition to the criticality of the fault, the size of the slip zone is also influenced by the size of the fault surface area affected by overpressure. The spatial extent of the largest slip increases with the spatial extent of the largest fluid pressure (Figure 4).
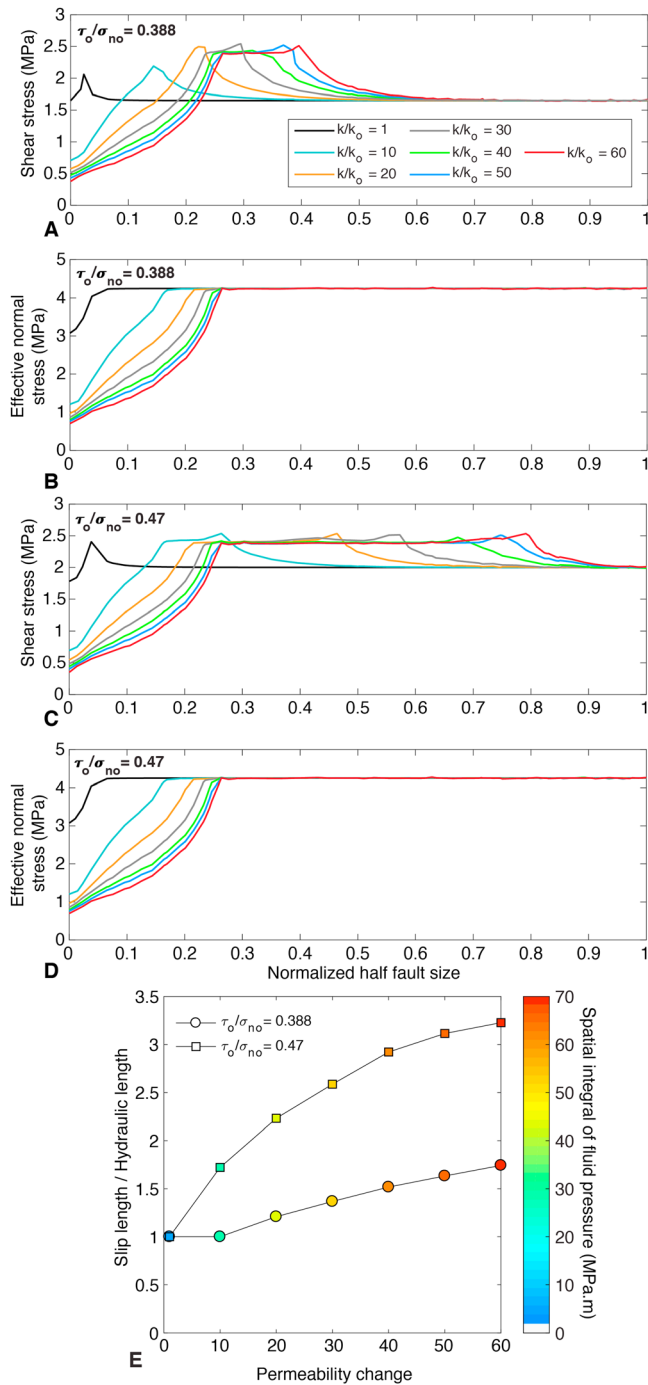
Figure 4. Half-profiles of (a–c) shear stress and (b–d) effective normal stress calculated along the fault for different changes in fault permeability and for two stress regimes, (a and b) $\tau_o/\sigma_{no} = 0.388$ and (c and d) $\tau_o/\sigma_{no} = 0.47$, respectively. The injection point is located at $x = 0$ along the horizontal axis. Half-profiles are plotted at the end of injection. (e) Maximum slip length over maximum hydraulic length as a function of permeability enhancement. The color bar and color points show the values of the spatial integral of fluid pressure (i.e., the size of the overpressurized fault surface area with $\Delta P > 0$) computed at the end of injection.

4. Discussion

Our results illustrate how the evolution of fault permeability may control the growth of aseismic slip relative to the fluid pressure diffusion. We show that the larger the fault permeability enhancement, the stronger is the growth of the aseismic slip zone. Indeed, our models with enhanced fault permeability show that the slip front significantly outpaces the fluid pressure diffusion (i.e., fluid pressure lags far behind rupture). Conversely, models with constant fault permeability fail to account for the fact that slip can grow beyond the fluid-pressurized patch. In this case, the slipping patch is slower or at the same rate than the diffusive growth of the pressurized zone. Through our investigations, we also find that aseismic slip initiates at the injection as a result of locally high fluid pressure, and then continues to develop within the pressurized zone and grow in a sustained manner beyond the pressure front. The slip causes local shear stress to increase, and because the strength of the fault can weaken with slip velocity, slip can propagate outside the pressurized zone without any further fluid pressure increase (Figures 4a–4d and S2). Thus, beyond the pressure front, stress perturbation and changes in frictional strength become dominant, providing the necessary conditions to drive the slip a significant distance beyond the pressure front. Moreover, when the fault is initially stressed to strength level close to the frictional limit (i.e., critically stressed fault), the effect of permeability enhancement is more pronounced and a large slip zone is simulated. Although our study focuses on "aseismic" slip, our results are consistent with previous studies of slip on a pressurized fault that, in some conditions, the "seismic" rupture can propagate beyond the pressurized zone (Galis et al., 2017; Garagash & Germanovich, 2012; Gischig, 2015). Although the criticality (τ_o/σ_{no}) of the fault is the critical parameter to growth of slip (Galis et al., 2017; Gischig, 2015), we showed that the permeability enhancement along a fault, which slips aseismically, is an additional effect that may help to amplify the effect of shear stress on faults optimally oriented for reactivation (i.e., critical stressed).

5. Implications and Concluding Remarks

The most general conclusion that can be drawn from our numerical models and experimental constraints of evolving fault permeability is that enhanced permeability favors the growth of aseismic slip beyond the pressurized area. The injection is local, but fault reactivation may propagate further. In our models, we observe two different mechanisms for fault activation: (1) Near the injection, where local fluid pressure is elevated, aseismic slip is mainly driven by the reduction of effective stress. The slip initiates when a sufficiently large fault patch is pressurized and weakened, which is significantly enhanced by the permeability increase with fault strain; (2) further away, in zones surrounding the pressure front, aseismic slip is driven by increased shear stress and frictional weakening (see Figures 4a–4d and S2). Indeed, failure in the pressurized fault patch increases the shear stress beyond the pressure front where the shear strength reduces as a function of the slip velocity. The reduction in fault strength is more pronounced in the pressurized zone than in the immediate surrounding region. These two distinct mechanisms may influence the rate of slip. In the pressurized zone, the effect of fault permeability enhancement is important during slow slip. It allows diffusing and homogenizing high fluid pressures over a large portion of the fault. When the slip rate accelerates, the influence of permeability diminishes.

Consequently, fluid pressure diffusion is not given sufficient time to equilibrate and drain away excess fluid pressure.

Moreover, the modeled progressive change in fault permeability with increasing fault displacements implies that aseismic slip may occur at large distances from injection, consistent with fluid activated aseismic slip observed in field experiments (Rivet et al., 2016) and at geothermal sites (Cornet, 2016; Hillers et al., 2015; Wei et al., 2015). Such fluid activated aseismic slip may then become a trigger mechanism for subsequent seismicity, as previously observed both in laboratory experiments (Goodfellow et al., 2015) and in small (i.e., meter) and large (i.e., kilometer) scale fluid injection experiments (Cornet, 2016; Guglielmi, Cappa, et al., 2015; Wei et al., 2015), as well as in modeling studies (Garagash & Germanovich, 2012). Thus, complementary to the frequently proposed mechanisms of fluid pressure diffusion (Keranen et al., 2014), poroelastic stressing (Goebel et al., 2017), and earthquake interactions (Schoenball & Ellsworth, 2017), aseismic slip may play a dominant role in triggering distant earthquake sequences beyond the targeted reservoir (e.g., Wei et al., 2015) and should be considered for seismic hazard assessment associated to fluid injection.

The fact that fluid-driven aseismic slip can develop beyond the zone immediately impacted by the injection has implications on the approaches for estimation of the maximum magnitude of injection-induced earthquakes. The most conventional methods assume that either the upper limit for seismic moment release is constrained by the pressure-induced stress change (deterministic approach of McGarr, 2014) or the ruptured area falls entirely within the pressurized volume (geometrical approach of Shapiro et al., 2011). Because seismic moments can be accommodated by aseismic slip in and outside the pressurized zone, including the contribution of stress changes due to aseismic slip in these deterministic and geometrical approaches would be beneficial in the estimate of maximum plausible magnitude of injection-induced earthquakes, M_{max}. Although it is difficult to distinguish between the aseismic and seismic regimes in data sets of observed induced seismicity, including the contribution of aseismic processes in the induced seismic hazard analyses through hydromechanical fault models would likely result in a lower maximum possible magnitude.

References

Baisch, S., Vörös, R., Rothert, E., Stang, H., Jung, R., & Schellschmidt, R. (2010). A numerical model for fluid injection induced seismicity at Soultz-sous-Forêts. *International Journal of Rock Mechanics and Mining Sciences*, *47*(3), 405–413. https://doi.org/10.1016/j.ijrmms.2009.10.001

Cappa, F., Guglielmi, Y., Rutqvist, J., Tsang, C.-F., & Thoraval, A. (2006). Hydromechanical modelling of pulse tests that measure fluid pressure and fracture normal displacement at the Coaraze laboratory site, France. *International Journal of Rock Mechanics and Mining Sciences*, *43*(7), 1062–1082. https://doi.org/10.1016/j.ijrmms.2006.03.006

Carpenter, B. M., Collettini, C., Viti, C., & Cavallo, A. (2016). The influence of normal stress and sliding velocity on the frictional behaviour of calcite at room temperature: Insights from laboratory experiments and microstructural observations. *Geophysical Journal International*, *205*(1), 548–561. https://doi.org/10.1093/gji/ggw038

Carpenter, B. M., Scuderi, M. M., Collettini, C., & Marone, C. (2014). Frictional heterogeneities on carbonate-bearing normal faults: Insights from the Monte Maggio Fault, Italy. *Journal of Geophysical Research: Solid Earth*, *119*, 9062–9076. https://doi.org/10.1002/2014JB011337

Catalli, F., Rinaldi, A. P., Gischig, V., Nespoli, M., & Wiemer, S. (2016). The importance of earthquake interactions for injection-induced seismicity: Retrospective modeling of the Basel Enhanced Geothermal System. *Geophysical Research Letters*, *43*, 4992–4999. https://doi.org/10.1002/2016GL068932

Cornet, F. H. (2016). Seismic and aseismic motions generated by fluid injections. *Geomech. Energy Environ.*, *5*, 42–54. https://doi.org/10.1016/j.gete.2015.12.003

Cundall, P. A. (1988). Formulation of a three-dimensional distinct element model—Part I. A scheme to detect and represent contacts in a system composed of many polyhedral blocks. *International Journal of Rock Mechanics and Mining Science and Geomechanics Abstracts*, *25*(3), 107–116. https://doi.org/10.1016/0148-9062(88)92293-0

Derode, B., Guglielmi, Y., De Barros, L., & Cappa, F. (2015). Seismic responses to fluid pressure perturbations in a slipping fault. *Geophysical Research Letters*, *42*, 3197–3203. https://doi.org/10.1002/2015GL063671

Dieterich, J. H. (1979). Modeling of rock friction experimental results and constitutive equations. *Journal of Geophysical Research*, *84*, 2161–2168. https://doi.org/10.1029/JB084iB05p02161

Duboeuf, L., De Barros, L., Cappa, F., Guglielmi, Y., Deschamps, A., & Seguy, S. (2017). Aseismic motions drive a sparse seismicity during fluid injections into a fractured zone in a carbonate reservoir. *Journal of Geophysical Research: Solid Earth*, *122*, 8285–8304. https://doi.org/10.1002/2017JB014535

Ellsworth, W. L. (2013). Injection-induced earthquakes. *Science*, *341*(6142). https://doi.org/10.1126/science.1225942

Galis, M., Ampuero, J. P., Mai, P. M., & Cappa, F. (2017). Induced seismicity provides insight into why earthquake ruptures stop. *Science Advances*, *3*(12), eaap7528. https://doi.org/10.1126/sciadv.aap7528

Garagash, D. I., & Germanovich, L. N. (2012). Nucleation and arrest of dynamic slip on a pressurized fault. *Journal of Geophysical Research*, *117*, B10310. https://doi.org/10.1029/2012JB009209

Gischig, V. S. (2015). Rupture propagation behavior and the largest possible earthquake induced by fluid injection into deep reservoirs. *Geophysical Research Letters*, *42*, 7420–7428. https://doi.org/10.1002/2015GL065072

Goebel, T. H. W., Hosseini, S. M., Cappa, F., Hauksson, E., Ampuero, J. P., Aminzadeh, F., & Saleeby, J. B. (2016). Wastewater disposal and earthquake swarm activity at the southern end of the Central Valley, California. *Geophysical Research Letters*, *43*, 1092–1099. https://doi.org/10.1002/2015GL066948

Goebel, T. H. W., Wiengarten, M., Chen, W., Haffener, J., & Brodsky, E. E. (2017). The 2016 M$_w$5.1 Fairview, Oklahoma earthquakes: Evidence for long-range poroelastic triggering at >40 km from fluid disposal wells. *Earth and Planetary Science Letters*, *472*, 50–61. https://doi.org/10.1016/j.epsl.2017.05.011

Goodfellow, S. D., Nasseri, M. H. B., Maxwell, S. C., & Young, R. P. (2015). Hydraulic fracture energy budget: Insights from the laboratory. *Geophysical Research Letters*, *42*, 3179–3187. https://doi.org/10.1002/2015GL063093

Guglielmi, Y., Cappa, F., & Amitrano, D. (2008). High-definition analysis of fluid induced seismicity related to the mesoscale hydromechanical properties of a fault zone. *Geophysical Research Letters*, *35*, L06306. https://doi.org/10.1029/2007GL033087

Guglielmi, Y., Cappa, F., Avouac, J.-P., Henry, P., & Elsworth, D. (2015). Seismicity triggered by fluid injections induced aseismic slip. *Science*, *348*(6240), 1224–1226. https://doi.org/10.1126/science.aab0476

Guglielmi, Y., Elsworth, D., Cappa, F., Henry, P., Gout, C., Dick, P., & Durand, J. (2015). In situ observations on the coupling between hydraulic diffusivity and displacements during fault reactivation in shales. *Journal of Geophysical Research: Solid Earth*, *120*, 7729–7748. https://doi.org/10.1002/2015JB012158

Hillers, G., Husen, S., Obermann, A., Planès, T., Larose, E., & Campillo, M. (2015). Noise-based monitoring and imaging of aseismic transient deformation induced by the 2006 Basel reservoir stimulation. *Geophysics*, *80*(4), KS51–KS68. https://doi.org/10.1190/geo2014-0455.1

Itasca Consulting Group (2016). 3DEC, 3-Dimensional Distinct Element Code. Itasca Consulting Group, Minneapolis, MN.

Jaeger, J. C., & Cook, N. G. W. (1979). *Fundamentals of rock mechanics*. London, U.K.: Chapman and Hall.

Jeanne, P., Guglielmi, Y., Lamarche, J., Cappa, F., & Marie, L. (2012). Architectural characteristics and petrophysical properties evolution of a strike-slip fault zone in a fractured porous carbonate reservoir. *Journal of Structural Geology*, *44*, 93–109. https://doi.org/10.1016/j.jsg.2012.08.016

Keranen, K., Weingarten, M., Abers, G. A., Bekins, B. A., & Ge, S. (2014). Sharp increase in Central Oklahoma seismicity since 2008 induced by massive wastewater injection. *Science*, *345*(6195), 448–451. https://doi.org/10.1126/science.1255802

Lengliné, O., Boubacar, M., & Schmittbuhl, J. (2017). Seismicity related to the hydraulic stimulation of GRT1, Rittershoffen, France. *Geophysical Journal International*, *208*(3), ggw490. https://doi.org/10.1093/gji/ggw490

Marone, C. (1998). Laboratory-derived friction laws and their application to seismic faulting. *Annual Review of Earth and Planetary Sciences*, *26*(1), 643–696. https://doi.org/10.1146/annurev.earth.26.1.643

McClure, M. W., & Horne, R. N. (2011). Investigation of injection-induced seismicity using a coupled fluid flow and rate/state friction model. *Geophysics*, *76*(6), WC,181–WC,198. https://doi.org/10.1190/geo2011-0064.1

McGarr, A. (2014). Maximum magnitude earthquakes induced by fluid injection. *Journal of Geophysical Research: Solid Earth*, *119*, 1008–1019. https://doi.org/10.1002/2013JB010597

Rivet, D., De Barros, L., Guglielmi, Y., Cappa, F., Castilla, R., & Henry, P. (2016). Seismic velocity changes associated with aseismic deformations of a fault stimulated by fluid injection. *Geophysical Research Letters*, *43*, 9563–9572. https://doi.org/10.1002/2016GL070410

Rubin, A. M., & Ampuero, J. P. (2005). Earthquake nucleation on (aging) rate and state faults. *Journal of Geophysical Research*, *110*, B11212. https://doi.org/10.1029/2005JB003686

Schoenball, M., & Ellsworth, W. L. (2017). A systematic assessment of the spatiotemporal evolution of fault activation through induced seismicity in Oklahoma and southern Kansas. *Journal of Geophysical Research: Solid Earth*, *122*, 10,189–10,206. https://doi.org/10.1002/2017JB014850

Scuderi, M. M., & Collettini, C. (2016). The role of fluid pressure in induced vs. triggered seismicity: Insights from rock deformation experiments on carbonates. *Nature Scientific Reports*, *6*(1), 24852. https://doi.org/10.1038/srep24852

Scuderi, M. M., Collettini, C., & Marone, C. (2017). Frictional stability and earthquake triggering during fluid pressure stimulation of an experimental fault. *Earth and Planetary Science Letters*, *477*, 84–96. https://doi.org/10.1016/j.epsl.2017.08.009

Shapiro, S. A., Krüger, O. S., Dinske, C., & Langenbruch, C. (2011). Magnitudes of induced earthquakes and geometric scales of fluid-stimulated rock volumes. *Geophysics*, *76*(6), WC55–WC63. https://doi.org/10.1190/geo2010-0349.1

Wei, S., Avouac, J. P., Hudnut, K. W., Donnellan, A., Parker, J. W., Graves, R., et al. (2015). The 2012 Brawley swarm triggered by injection-induced aseismic slip. *Earth and Planetary Science Letters*, *422*, 115–125. https://doi.org/10.1016/j.epsl.2015.03.054

Witherspoon, P. A., Wang, J. S. Y., Iwai, K., & Gale, J. E. (1980). Validity of cubic law for fluid flow in a deformable rock fracture. *Water Resources Research*, *16*, 1016–1024. https://doi.org/10.1029/WR016i006p01016

Zang, A., Oye, V., Jousset, P., Deichmann, N., Gritto, R., McGarr, A., et al. (2014). Analysis of induced seismicity in geothermal reservoirs—An overview. *Geothermics*, *52*, 6–21. https://doi.org/10.1016/j.geothermics.2014.06.005